

MILLIMETERWAVE WIRELESS CHANNEL MEASUREMENTS
WITH A CHANNEL SOUNDER

IN PARTIAL FULFILLMENT OF THE REQUIREMENTS
FOR THE HONOR THESIS

Yijun Qiao
April 2012

Abstract

Research in inexpensive millimeter wave devices and electronically steerable antennas forbodes future high speed communications that use carrier frequencies at millimeterwave frequencies such as 38 and 60 GHz. At these frequencies, the available RF bandwidth is much greater than that of current 4G systems, resulting in massive amounts of data rates, and high gain millimeterwave steerable antennas can be much smaller than antennas at current frequencies. As the carrier frequency is increased, behaviors of the wireless signals in different environments need to be better understood. The thesis presents results from an extensive channel measurement campaign for peer-to-peer, peer-to-vehicle, and rooftop-to-ground (base station-to-peer) propagation measurements with a sliding correlator channel measurement system at 38 GHz or 60 GHz carrier frequencies in an outdoor urban campus environment using directional and mechanically steerable antennas. This work provides angle of arrival (AOA) and channel characteristics for directional antenna beams that may exploit non-line-of-sight propagation paths for futuristic channels at 38 GHz and 60 GHz. The thesis also includes descriptions of an antenna positioning track that was designed to assist in future channel measurements. The track enables automatic mechanical steering in an antennas azimuth angle and horizontal position, and manual mechanical steering in elevation angle, polarization, and vertical positions. Details on the track design, design concerns, parts, as well as the tracks control software are provided.

Acknowledgements

The research would not have been possible without the continual supports and encouragements of Professor Theodore S. Rappaport, Professor Robert W. Heath Jr., and Professor Jeffrey Andrews. I would also like to thank Eshar Ben-Dor, James Murdock, Samuel Lauffenburger, Travis Forbes, Felix Gutierrez, Adrian Duran, and Jonathan Tamir for their assistance.

Contents

Abstract	iv
Acknowledgements	v
1 Introduction	1
2 The Measurement System	3
2.1 System Architecture	3
2.2 Calibration and Post-processing	6
3 General Measurement Procedure	8
4 Measurement Scenarios	9
4.1 60GHz Peer-to-peer and Peer-to-vehicle Measurement Scenarios	9
4.2 38GHz Rooftop-to-ground Measurement Scenarios	11
5 Data Presentation and Analysis	13
5.1 60GHz Peer-to-peer and Peer-to-vehicle Results	13
5.2 38GHz Rooftop-to-ground Results	17
6 Receiver Antenna Positioning Track	23
6.1 Design	23
6.2 Track Components	25
6.3 A Mechanical Concern: Torque	28
6.4 Track Software	31
6.5 Automatic Signal Scanning	34
7 Future Works	35

8 Conclusion	36
9 Published Works	38
Bibliography	39

Chapter 1

Introduction

The proliferation of wireless services and technologies has resulted in a global bandwidth shortage, as wireless carrier-frequencies have been restricted to the frequency band from 800 MHz to 5.8 GHz [1]. There is growing interest in the use of wireless millimeter-wave frequencies with carrier frequency greater than 30 GHz, where massively available bandwidth exceeds the combined bandwidths of all wireless communication systems in widespread use today [1].

Some of the earliest uses of millimeter-wave frequencies were Local Multipoint Distribution System (LMDS) and Backhaul services at 20 and 40 GHz in the 1990s, but these were commercially unsuccessful due to high hardware costs associated with millimeter-wave devices. Advancements in CMOS production technologies, however, have led to great cost and size reductions of these devices, making millimeter-wave frequencies an attractive and now cost-effective means of alleviating the bandwidth crisis. Devices such as smart antenna arrays and low power wide spectrum millimeter wave circuits may soon become prevalent as industry leaders look to millimeter-wave frequencies as a means to continue wireless technological development in the coming decades [2],[3].

Understanding radio channel propagation characteristics at these millimeter wave frequencies is crucial for the design of future communication systems [4], [5]. Several have measured the outdoor propagation environment at millimeter wave frequencies focusing on LMDS applications, which involve elevated and stationary antennas. In [6], [7], and [8], channels were measured during regular, rain, and hail conditions at various ranges and frequencies.[9] and [10] noted that propagation obstacles, including tree canopies and rooftops, can limit throughput at millimeter wave frequencies, and contended that line-of-sight (LOS) paths may be the only viable means for sufficient

signal strength. Little else is known about outdoor multipath characteristics for very broadband mm-wave channels having 1 GHz or more of bandwidth, yet such information is essential for the design of futuristic broadband devices with adaptive antennas that are certain to emerge [1], [11]. Also, none of the previous studies examined the millimeter wave outdoor channel for cellular applications.

This thesis discusses results from various 38GHz and 60GHz channel measurements with angle-of-arrival information using a broadband spread spectrum sliding correlator measurement system taken at The University of Texas at Austin campus. Measurement scenarios include peer-to-peer, peer-to-vehicle, and rooftop-to-ground (basestation-to-peer). The work shows insight into the wireless channel behavior with 38GHz and 60GHz carrier frequencies. In addition, an antenna positioning track system designed to ease the measurement process is presented.

Chapter 2

The Measurement System

A 400 Mega-chips-per-second (Mcps) or 750 Mcps spread spectrum sliding correlator is used to measure the wireless channels behaviors at 38 GHz or 60 GHz carrier frequencies, respectively. The system was introduced by Donald Cox in the early cellular channel measuring days [12], and its low cost and ease of implementation, mobility, and ability to reject narrowband noise are the main advantages. In this section, the sliding correlator's system architecture and theory of operation, calibration procedures, and post processing procedures are discussed.

2.1 System Architecture

The detailed system architecture of a 59.4 GHz sliding correlator channel sounder can be seen in Figure 2.1. At the transmitter side, a Pseudorandom Noise (PN) sequence running at chip rate R_c is mixed (multiplied) with a sinusoidal signal running at an intermediate frequency IF of 5.4 GHz. The resultant signal is further mixed with a $5.4 \times 10 = 54$ GHz sinusoidal wave, resulting in a signal with center frequency of 59.4 GHz, which is transmitted through the transmitter antenna. Due to the frequency limitations of each components, the harmonics from the mixing operation are attenuated without the need of a filter.

When the receiver side receives the environment corrupted signal, the signal is downconverted to IF at 5.4 GHz, separated into In-phase and Quadrature phase (I and Q) channels. The I and Q channel signals are created by first splitting the IF signal with a splitter and mixing two sinusoids separated in phase by 90° generated by a LO and a 90° phase shifter. Each I or Q channel is then mixed with a slightly slower chip rate R'_c but otherwise the same PN sequence as the PN sequence from the

transmitter. The resulting signals in I and Q channel are passed through an analog lowpass filter with cutoff frequency $R_c - R'_c$. The data from I and Q channels are then sent to a National Instrument(NI)s data acquisition board (DAQ) connected to a laptop. The laptop processes and saves the data it reads in with a LabVIEW program.

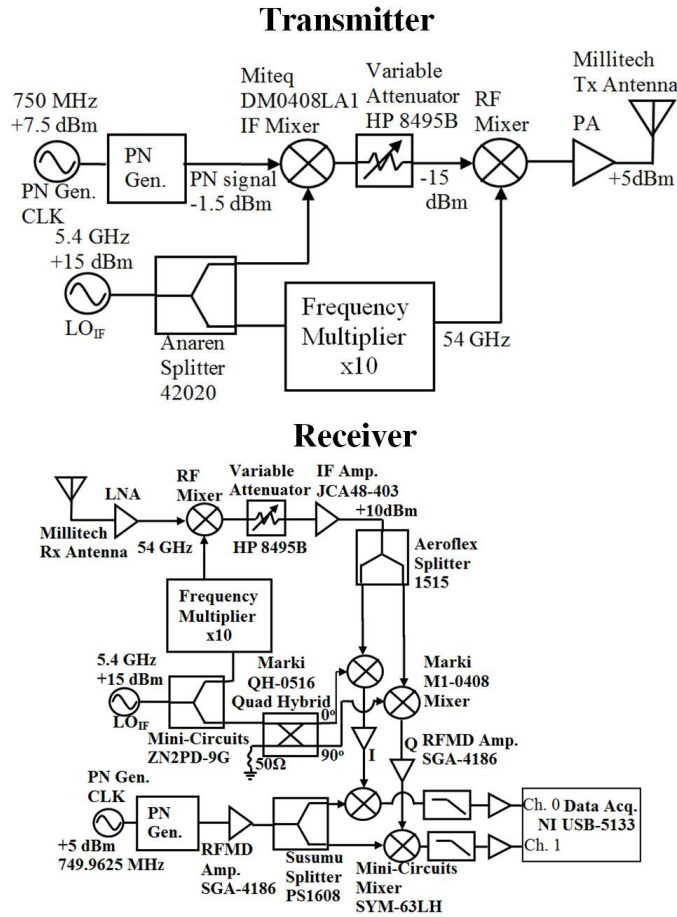


Figure 2.1: Detailed block diagram of the channel sounder operating at 59.4 GHz using a 750 Mcps PN Generator.

The simplified system architecture shown in Figure 2.2 can help to explain the theory of operation of a sliding correlator. At the transmitter, signal from a signal generator is mixed with a PN sequence to provide clock for the PN. For the system used for this reserach, the signal generator outputs a sinusoidal wave at frequency R_c . The result, a PN running at clock rate R_c , is amplified and sent through an antenna

(the upconversion part is omitted). Note that the frequency domain representation of a sinusoidal wave is an impulse (narrowband), while the representation of the PN sequence is a sinc function (wideband) with a null to null bandwidth of $2 \times R_c$. The mixing operation spreads the a narrowband signal into a wide band signal, since multiplication in time is convolution in frequency domain.

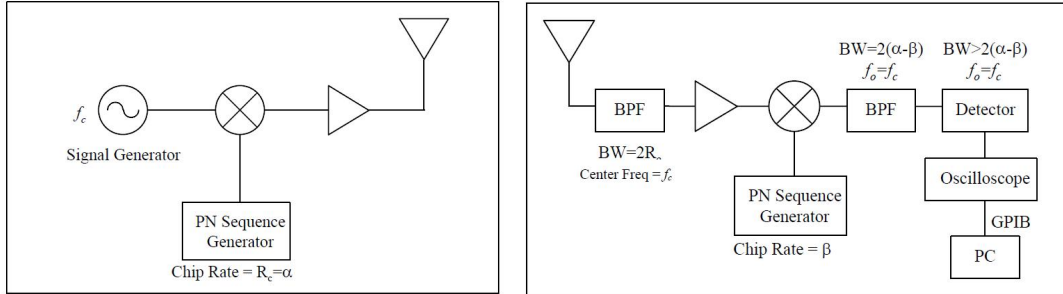


Figure 2.2: Simplified system architecture [13]. Left: Transmitter block diagram. Right: Receiver block diagram.

The signal sent from the transmitter antenna is sent through the environment and received by the receiver (the down-conversion part is omitted). The bandpass filter (BPF) serves to cut off out-of-band interference. Then the spread signal from the transmitter is amplified and de-spread by correlating it with the same PN sequence at the receiver. By letting the receiver-side PN sequence run at a slightly slower speed, the faster transmitter-side PN sequence will slide past the receiver-side PN sequence. As the two PN sequences slide, they are also multiplied and bandpass filtered, which performs an integration operation continuously. Combining the slide and integration processes, correlation is achieved. The resultant waveform shows a peak (approximately a δ function) only when the two PN sequences line up. After correlation, the signal sent to NI's DAQ is converted to a digital form through sampling and detected, displayed, and saved through a LabVIEW program. Due to reflection, refraction, and scattering in the environment, the sent signal will have copied versions of it arriving at different times with different amplitudes. These delayed PN sequences will correlate with the receiver PN at different times, so their correlated peaks with various amplitudes will show up at a later time than the first arriving PN signal (which is from the Line-Of-Sight wave). Values of channel parameters including path loss and delay spread can be extracted from the received signal.

2.2 Calibration and Post-processing

A power-delay-profile (PDP) is a plot of received signal power versus time. The purpose of system calibration is to empirically obtain a linear relationship between true received power and area under unprocessed-PDP, as well as finding the linear range of the system. The unprocessed PDP is a plot of signal voltage vs. time displayed on the oscilloscope on the receiver. By changing the amount of attenuation on a variable attenuator at the receiver and observing the area (found by summing all samples) under the unprocessed-PDP, a linear relationship of true received power (dBm) vs. area $Area_{measured}$ under an unprocessed-PDP and can be obtained. Calibration is a required step before post processing, and calibration must be done every time before conducting set of measurements to ensure the system works properly (i.e. the linear range is approximately the same between sets of measurements, and inside the linear range, every 1 dB of attenuation at the attenuator results in approximately 1 dB of reduction in received signal power).

A Matlab program was used for post processing each set of $I[n]$ and $Q[n]$, which are sampled data of the I and Q channels at the output of the NI DAQ. The n represents the index for the samples. The program first combines $I[n]$ and $Q[n]$ using the equation $I^2[n]+Q^2[n]$. The combined signal is passed through a low pass Butterworth filter with cutoff frequency $R_c - R'_c$, outputting $PDP_{temp}[n]$. Although an analog low pass filter already filters at such frequency in the correlator unit, this second digital filter has a sharper filter cutoff transition region. As a result, the output of the digital low pass filter is much smoother than the input. Each sample of $PDP_{temp}[n]$ is then multiplied by the slope read from the ($Received\ Power \times Area_{measured}$) graph obtained by calibration. Each sample is then multiplied by the sampling rate (per nanosecond) f_s of the DAQ. The result is an array $PDP[n]$ in dBm/ns, which is plotted against time in ns. Note that for every long sequence of PN sent, an impulse is output, so a time dilation exist at the raw received signal. That is, the observed time at the oscilloscope is not the true propagation time. Therefore, the horizontal time axis nT_s of PDP_{temp} needs to be divided by $R_c - R'_c$ to restore true propagation time., where T_s is $\frac{1}{f_s}$. This plot of power/time vs. time is the desired PDP.

With the PDP, RMS delay spread and mean excess delay can be calculated. Define $\tau[nT_s]$ = true undilated excess delay of multipath at the n^{th} sample, the mean excess delay can be found using equation:

$$\bar{\tau} = \frac{\sum_n \tau[nT_s] \times PDP[n]}{\sum_n PDP[nT_s]}.$$

The numerator is the standard expected value formula which in this case interprets $PDP[n]$ as a probability density function, and the denominator is used to normalize the area under PDP to 1 (so that it meets the requirement to be a probability density function). The second moment is then calculated by the equation:

$$\bar{\tau}^2 = \frac{\sum_n \tau^2[nT_s] \times PDP[n]}{\sum_n PDP[nT_s]}.$$

The RMS delay spread is now calculated by:

$$\sigma = \sqrt{\bar{\tau}^2 - (\bar{\tau})^2}.$$

The pass loss (in dBm) can be calculated with the equation:

$$Path\ Loss = -(P_R - P_T - G_T - G_R),$$

where P_R is the received power right after the receiver antenna, P_T is the transmitted power right before the transmitter antenna, G_T is transmitter antenna gain, and G_R is the receiver antenna gain. The minus sign makes path loss a positive value.

Chapter 3

General Measurement Procedure

Highly directional antennas at the transmitter and receiver enable scanning off-boresight in both azimuth and elevation angular directions to establish detectable links, similar to an electrically steerable antenna array. At each receiver location, measurements were conducted for one to fourteen unique transmitter-receiver antenna angle combinations that resulted in links. For the LOS and partially obstructed (the obstruction might be from leaves or handrails) LOS links, the transmitter and receiver antennas were manually steered to point toward each other. The NLOS links were found using a manual steering approach. First, the transmitter antenna was steered toward a potential scatterer, such as a lamppost, building, tree, or automobile. Next, the receiver antenna was steered along its azimuth and elevation planes to search for a signal. At every location, each measurement was formed by spatially averaging PDPs from eight local positions at the measurement location equally spaced by 10 along a circular track. At each position on the track, the receiver antenna was slightly reoriented to consistently point toward the believed cause of the received signal (e.g. to a reflecting building or lamppost). Each acquired PDP for each local position on the circular track was the result of averaging 20 PDPs acquired by software in rapid succession over a few seconds. After the spatial averaging of the local position PDPs, the average PDP was manually thresholded at the noise floor to distinguish between channel-induced multipath and noise when computing channel statistical parameters.

Chapter 4

Measurement Scenarios

Two sets of measurements to characterize the wireless propagation channel of an urban campus environment are presented here. This includes 60GHz peer-to-peer and peer-to-vehicle measurements and 38GHz rooftop-to-ground measurements. All measurements were done on the University of Texas at Austin campus.

4.1 60GHz Peer-to-peer and Peer-to-vehicle Measurement Scenarios

Measurements were made using the sliding correlator at 60 GHz carrier frequency to measure outdoor wireless channel in two urban campus environments. Both the transmitter and receiver used identical 25dBi highly directional horn antennas. The 60GHz peer-to-peer is an outdoor courtyard with pedestrian walkway between several buildings on The University of Texas campus. The courtyard has some vegetation and several lamp poles and is surrounded by tall office buildings 6 to 10 stories high. Metallic objects, such as the aluminum siding of buildings and lamp posts, were found to be reflective and could reliably produce a NLOS link. Several metallic objects present in the first measurement environment are circled in Figure 4.1. The transmitter and receiver antennas were separated by 18.5 m. Ten receiver locations with T-R separation distances between 17.8 m and 117.8 m in the courtyard were used, as they represented typical pedestrian locations near buildings and on the sidewalk and always provided a LOS path between Tx and Rx. At each of the ten locations, there was at least four, and at most six, different transmitter and receiver antenna orientations (including the LOS antenna pointing orientation) resulted in a detectable link between the transmitter and the receiver.



Figure 4.1: Photo of 60GHz urban campus measurement location with surrounding buildings, trees, light posts, and handrails. Metallic objects, circled in the photo, were found to be useful reflectors that can be exploited in non-LOS conditions.

The second set of measurements explored the peer-to-vehicle measurement scenario. The receiver antenna was placed inside a mid-sized sedan automobile (2003 Mitsubishi Galant) located at distances of 4, 12, and 23 meters away from the standalone transmitter. The transmitter-to-receiver (T-R) separation distances were chosen to approximate the separation of a lane of traffic, a two way street, and a multi-lane highway [14]. Measurements were taken at a parking lot on The University of Texas campus with the vehicle facing a multistory building. Figure 4.2 shows the measurement environment and setup, where the transmitter antenna was 1.5 m above ground and the receiver antenna was at head level for a seated passenger in the car. The scenario was designed to determine the characteristics of LOS propagation and of the link generated by reflecting off the passengers in the vehicle at 60 GHz. Measurements were made with two passengers in the vehicle, where the receiver antenna was placed at head level at two different locations within the vehicle, corresponding to locations of the driver and a rear passenger, as shown in Figure 4. The measurement procedure differed slightly from that described in section III. The outdoor transmitter antenna was directly pointed in the direction of the vehicle with a fixed orientation, while the in-vehicle receiver horn antenna was swept across the entire horizon to find LOS and NLOS links. Measurements showed that NLOS links could be made when the receiver antenna pointed toward the seated passengers, while other orientations resulted in undetectable signals.

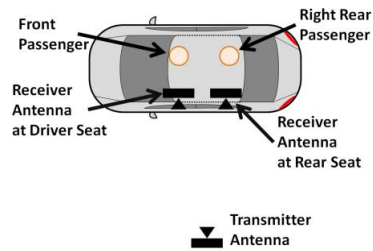


Figure 4.2: Top view of the vehicle measurement set-up. The receiver was placed inside the vehicle at each of the two locations shown, where non-LOS paths were identified by rotating the receiver antenna. Passengers were seated at the front and right rear passenger seats shown by the circles in the bottom diagram.

4.2 38GHz Rooftop-to-ground Measurement Scenarios

For the 38GHz Rooftop-to-ground measurements, the transmitter was placed at four locations within The University of Texas at Austin campus. The specific locations are labeled and shown in Figure 4.3. The transmitter used a 25 dBi horn antenna, while the receiver used both 25 dBi and 13.3 dBi horn antennas. At each location, the transmitter antenna was mounted on a tripod 1.5 m above the roof toward the buildings edge. The first two transmitter locations were along the northern and eastern edges of the rooftop of an eight-story building (36 m). The third location was on the northern edge of a five-story rooftop (23 m). The last transmitter location was closer to the ground, at approximately 8 meters above a recessed parking lot and busy four lane avenue. For each transmitter location, about eleven receiver positions were chosen for measurements with the 25 dBi receiver antenna, and about five of the locations for each transmitter position were revisited and measured with the 13.3 dBi receiver antenna. The receiver locations represented typical outdoor urban cellular environments, in which a user may have clear LOS to the transmitter, partially obstructed LOS due to foliage, or NLOS due to buildings or other large obstructions. The 25 dBi receiver antenna locations ranged from 29 m to 930 m from the transmitter. The 13.3 dBi antenna locations were between 70 m and 728 m from the transmitter.

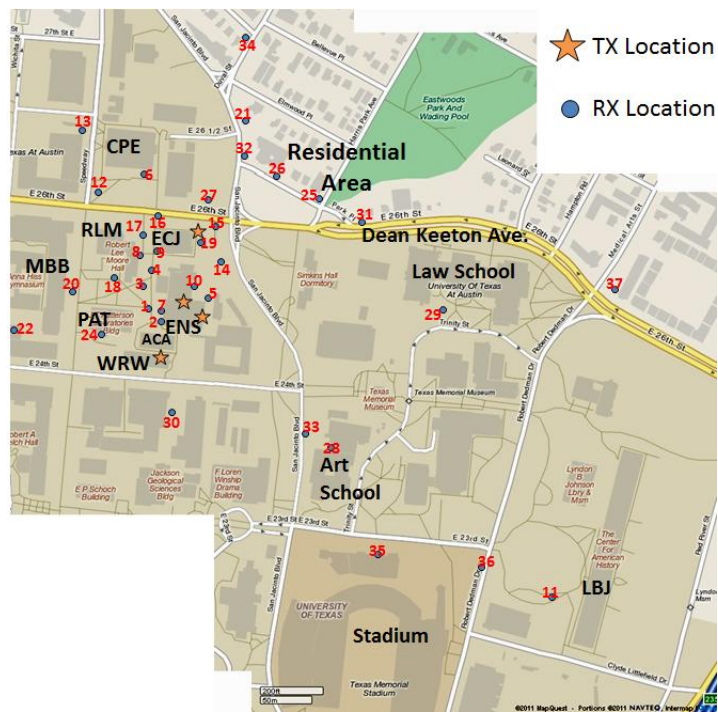


Figure 4.3: Detailed map of transmitter and receiver locations used for 38GHz rooftop-to-ground measurements.

Chapter 5

Data Presentation and Analysis

During all measurements, the transmitter and receiver antenna azimuth and elevation angles and power delay profiles (PDP) are recorded. The results shown below are summaries of these data for both 60GHz and 38GHz measurement scenarios.

5.1 60GHz Peer-to-peer and Peer-to-vehicle Results

The top of Figure 5.1 shows an example of received power versus receiver azimuth rotation angle for 60 GHz measurements with a T-R separation of 18.5m. The Figure contains curves for three transmitter antenna orientations. The boresight orientation (0°) represented by the blue line, which has the transmitter pointing directly towards the receiver antenna, contains two main peaks received by the receiver. The first, as expected, occurs when the antennas face each other and a second peak when the receiver faces the opposite direction from the transmitter (at 180°). The peak at 180° was verified to originate from a light post that stood in-line with the transmitter.

Represented by the red line, a -30° transmitter beam heading caused the transmitter to point toward a metallic railing and several trash cans. A peak is seen in Figure 6 when the receiver antenna was pointed at 40° toward those same objects. PDPs for typical LOS and NLOS antenna orientations are shown (bottom of Figure 5.2) with the NLOS orientations exhibiting a higher multipath spread and lower received power. This result, which was typical, shows the requirement of metallic objects in order to exploit NLOS communications at 60 GHz with beam steering. It is important to note that at most T-R pointing angle combinations, NLOS links are too weak or do not exist.

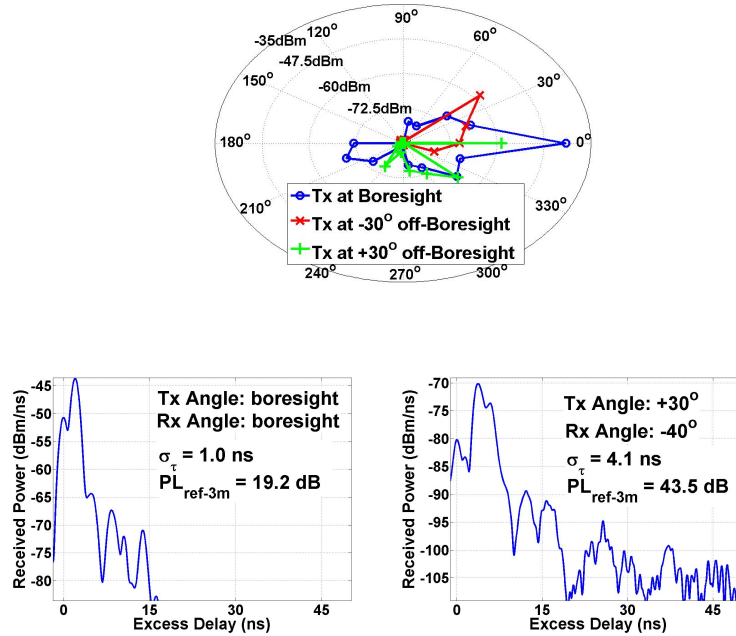


Figure 5.1: (Top) Angle of arrival 60GHz measurements from the campus courtyard show received power versus receiver antenna rotation angle in azimuth direction for three transmitter antenna orientations. (Bottom) A typical LOS and NLOS PDP demonstrate the typical increase in multipath spread and path loss when transmitter and receiver antennas are not pointed at each other.

Path loss data for all ten of the measured courtyard locations were calculated with respect to a 3 meter free space reference as seen in Figure 5.2. A MMSE best fit path loss model for LOS courtyard measurements yielded a path loss exponent of $n = 2.23$. NLOS antenna pointing conditions, where transmitter and receiver antennas were each pointed to find reflective objects (much as adaptive antennas would do), were found to have a path loss exponent of $n = 4.19$. Typical NLOS paths are weaker than LOS paths by 15 to 40 dB.

PDPs were acquired for several passenger configurations and antenna locations at LOS conditions within an automobile. Figure 5.2 contains path loss data for the vehicular measurements. The average path loss exponent for LOS vehicle environments within a 23 m T-R range ($n = 2.66$) is slightly higher than that of the pedestrian walkway. It is interesting to note that the windows of the vehicle were raised during measurements, and an offset attenuation of about 6dB was observed for the vehicle

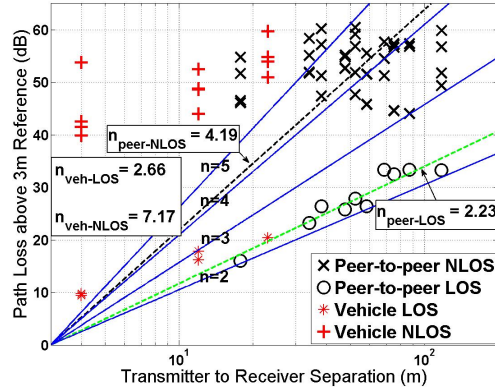


Figure 5.2: 60GHz Path loss scatter plot for peer-to-peer and vehicle environments. LOS measurements with antennas pointing at each other provide $n = 2.23$ ($= 1.87\text{dB}$) and 2.66 ($= 5.4\text{dB}$) for peer-to-peer and vehicle environments, respectively. When measurable, NLOS paths have $n = 4.19$ ($= 9.98\text{dB}$) and 7.17 ($= 23.8\text{dB}$), respectively, for the courtyard and into a vehicle.

LOS results with windows up. This is reasonable when compared to 60 GHz penetration loss results for glass [15], and explains slightly higher LOS path loss. The NLOS antenna pointing paths yielded a very high path loss exponent of $n=7.17$ due to the shielding effect of the car body, and RF absorption inside the vehicle. Scattering from passengers provided some propagation but at much weaker received power levels in NLOS vehicle situations than LOS propagation paths into the vehicle.

For the pedestrian courtyard, LOS channels always had the first arriving signal much stronger than the later-arriving multipath, and had minimal RMS delay spread (less than 0.9 ns). In contrast, non-LOS antenna pointing situations had highly variable RMS delay spreads, with 7.39 ns mean RMS delay spread, and a maximum of 36.6 ns. This same trend was found in the vehicle measurements, where non-LOS antenna pointing paths reached a maximum delay spread of 12.3 ns.

A CDF plot (Figure 5.3) illustrates the RMS delay spread data. While several high delay spread measurements were found, the large majority of measured paths had delay spreads below 10 ns. The variation of the RMS delay spread as a function of distance is seen in the scatter plot of Figure 5.4. The plot shows that high delay spreads are less likely at very large T-R separations ($>50\text{m}$). This can be explained by the high absorption of signal energy by oxygen molecules in the air in general at 60 GHz, which serves to reduce the number of observable multipath components

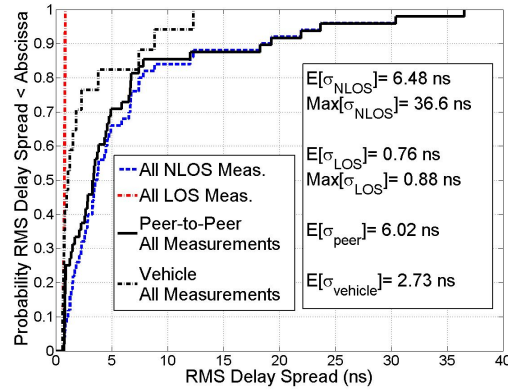


Figure 5.3: Cumulative distribution function (CDF) of the RMS delay spread at 60 GHz measured in a campus outdoor environment in a pedestrian courtyard and within a vehicle. The CDFs for LOS and NLOS links in those locations are distinguished by low spreads in LOS, and highly variable spreads for cases where Tx and Rx antennas were not pointed at each other.

when directional antennas are used. It is only when smooth objects are illuminated by both the transmitter and receiver that longer distance NLOS links can be made.

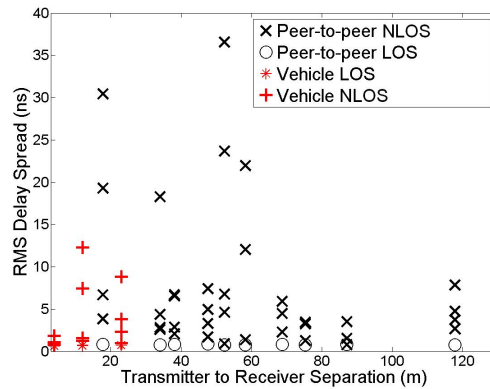


Figure 5.4: Scatter plot of RMS delay spread vs. T-R separation for peer-to-peer communications in a courtyard and from a vehicle. NLOS antenna pointing paths have lower RMS delay spread than LOS paths due to the high path loss at 60 GHz.

5.2 38GHz Rooftop-to-ground Results

The excess path loss and RMS delay spread were computed for all 731 measurements recorded in the campaign. Excess path loss was calculated with respect to a five meter free space reference. The path-loss exponents for the clear LOS, partially obstructed LOS, and NLOS measurements were separately computed to compare the characteristics of obstructed and NLOS paths to the characteristics of clear LOS links for which no clutter or vegetation existed between the transmitter and receiver.

Figure 5.5 shows a scatter plot of the path loss above 5 m free space reference (i.e. relative path loss) for each measurement acquired using the 25 dBi receiver antenna. The clear (i.e. no clutter or vegetation between the transmitter and receiver) LOS path loss exponent is 1.89, slightly below that of free space, and increases to 2.30 when partially obstructed LOS links are also considered. In contrast, the NLOS measurements are weaker than LOS paths by 10 to 30 dB and have a path loss exponent of 3.86. If only the best NLOS links at each location are considered (to mimic the performance of an adaptive antenna array that searches for the best link available), the path loss exponent is reduced to 3.2.

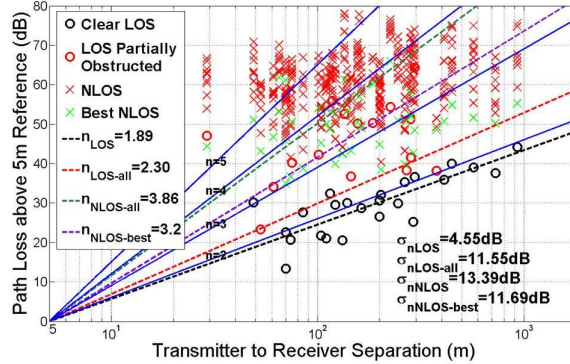


Figure 5.5: Path loss scatter plot using 25dBi Rx antenna at 38 GHz. LOS and NLOS measurements have path loss exponents of 2.30 and 3.86, respectively, while the best NLOS links have a path loss exponent of 3.2.

Figure 5.6 shows the path loss scatter plot for the measurements acquired using the wider beam 13.3 dBi receiver antenna. The path loss exponents for clear LOS and both clear and partially obstructed LOS are 1.90 and 2.21, respectively, while the exponent for NLOS measurements is 3.18. The best NLOS paths have an exponent of 2.56. Notably, the 13.3 dBi receiver antenna provides lower path-loss exponents for obstructed and NLOS links, in comparison to measurements obtained with the 25

dBi receiver antenna. The low NLOS path loss was caused by the remnant energy received from the LOS direction path due to the large beamwidth and fewer captured links above 60dB relative path loss due to the lower antenna gain. The path loss exponent observed for obstructed boresight direction links (i.e. partially obstructed LOS) was slightly lower due to the increase in scattering and diffracting paths which were captured by the receiver antenna.

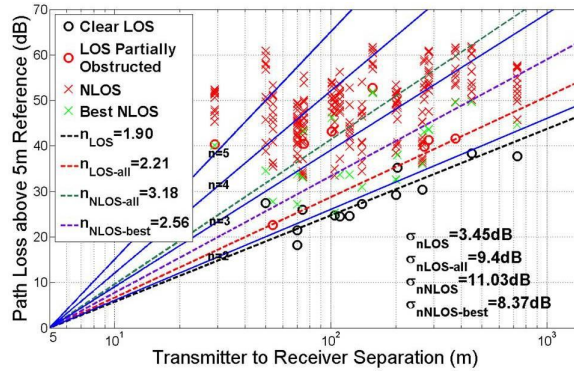


Figure 5.6: Path loss scatter plot using 13.3 dBi RX antenna at 38GHz. Lower NLOS and partially obstructed LOS path loss exponents were observed due to increase in scattering and diffracting links captured by a wider beam antenna.

The CDFs of the RMS delay spreads for LOS and NLOS paths using each receiver antenna are shown in Figure 5.7. The delay spreads with each antenna were nearly identical in distribution, despite the discrepancy in NLOS path loss. Most LOS measurements had the minimal RMS delay spread, on the order of 1.1 ns due to the pulse shape, with one partially obstructed LOS link resulting in a maximum of 15.5 ns. The NLOS measurements exhibited higher and more varied delay spreads, with a mean of 14.3 ns (for 25 dBi receiver antenna) and 13.7 ns (13.3 dBi receiver antenna). The maximum NLOS RMS delay spreads were 255 and 166 ns for 25 and 13.3 dBi receiver antennas, respectively. Nonetheless, more than 80% of the NLOS links had RMS delay spreads under 20 ns.

RMS delay spread as a function of excess path loss (i.e. path loss in excess of the predicted free space loss) is shown in Figure 5.8. As seen, weaker signals had probabilistically higher delay spreads, since multipath components become more prominent for weaker signals. However, the relationship between RMS delay spread and path loss was site-specific, as shown by the wide range of RMS delay spreads. For both antenna configurations, the RMS delay spread initially increases with excess loss

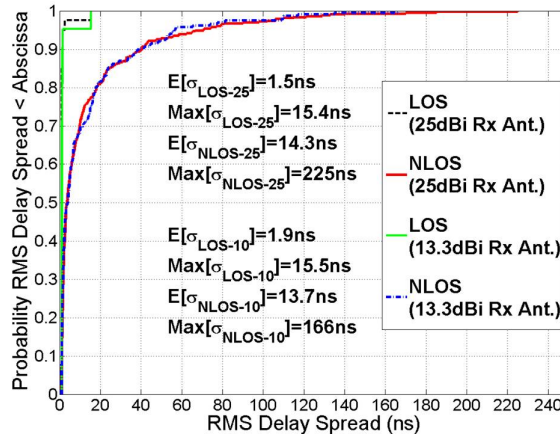


Figure 5.7: RMS delay spread CDF for all 38GHz measurements. Measurements using 25dBi and 13.3dBi antennas show nearly identical delay spread CDFs.

and subsequently falls slowly. The peak RMS delay spreads occur at a lower excess loss for the 13.3 dBi antennas than the 25 dBi counterpart due to their lower gain. A low gain antenna is capable of capturing energy from more directions, yet fewer of the arriving multipath components are above the system sensitivity. Thus, the RMS delay spread depends on the trade-off between antenna gain, which limits the number of multipath components above the sensitivity level as antenna gain decreases, and beamwidth, where higher beamwidths result in more collected paths.

RMS delay spreads for the 25 dBi and 13.3 dBi receiver antennas are plotted as a function of TR separation in Figure 5.9. Generally, delay spread and TR separation are inversely proportional. As the separation increases, the signal strength decreases, thus multipaths drop below the minimal detectable signal level, lowering the RMS delay spread. This may play a role in future system design, as directional antennas can be used to maintain a low-interference link over large distances, yet less diversity can be exploited in a MIMO setting.

Figure 5.10 shows the RMS delay spread as a function of combined antenna pointing angles, where the combined angle at each measurement is the sum of absolute transmitter and receiver azimuth angles off boresight plus the sum in elevation angle between the transmitter and receiver antennas. The elevation angle sum is zero when the antennas are pointing in the boresight direction. As expected, RMS delay spread increases with combined angle, as steeper angles are correlated with a higher number of signal bounces from the transmitter to the receiver. At small angles, both antennas exhibit low variance in delay spread.

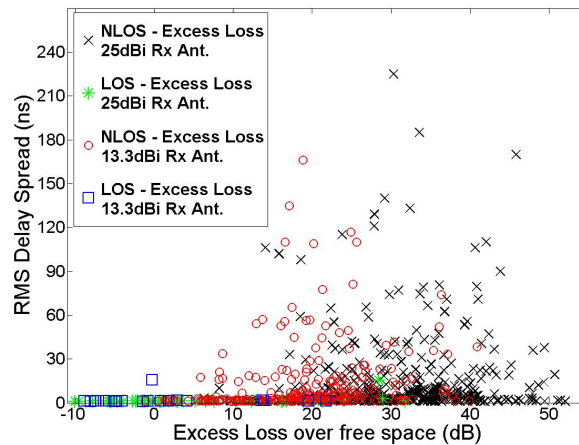


Figure 5.8: RMS delay spread vs. excess path loss above free space predicted loss for 38GHz. Weak signals exhibit high delay spreads as weak multipath become important.

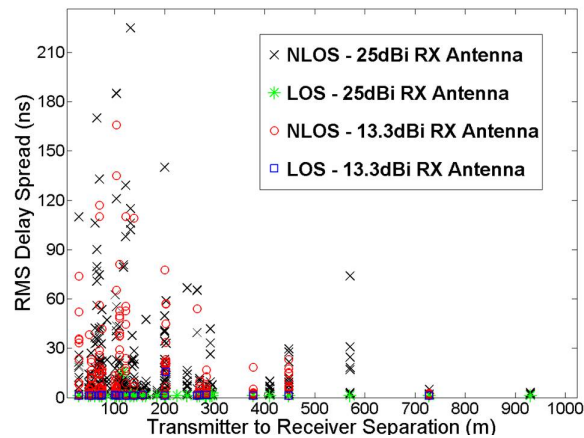


Figure 5.9: RMS delay spread as a function of TR separation at 38GHz. Delay spread decreases over long paths since multipath drops below system sensitivity.

As seen in Figure 5.9 and Figure 5.10, RMS delay spread is inversely proportional to TR separation distance and directly proportional to combined off-boresight angle. To study the importance of these two opposing trends, the arc length of a particular measurement is defined as the product of the TR separation and the combined off-boresight angle (in radians). Figure 16 shows RMS delay spread vs. arc length over

all measurements. As the plot shows, there is an inverse relationship on a large scale from 0 to 3000 m-rad. This decreasing trend matches that of Figure 5.9, indicating that TR separation distance is more important than off-boresight angle over large arc-lengths in determining RMS delay spread. However, a close-up of the plot for values below 300 m-rad suggests an opposite trend. In fact, at low arc lengths, the plot resembles Figure 5.10, implying that the combined off-boresight angle is of higher importance. The transition point for this urban campus environment occurs at approximately 400 meter-radian, where distance begins dominating angle.

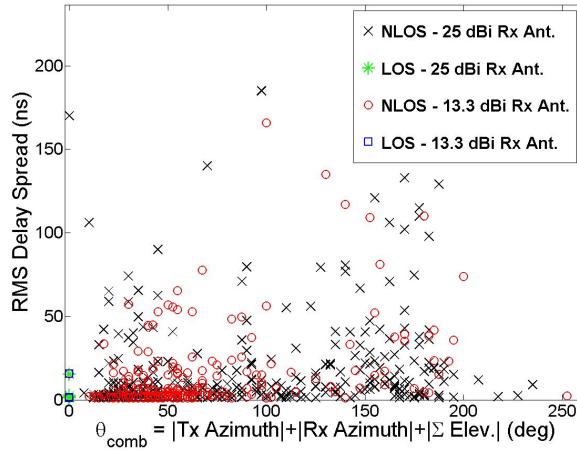


Figure 5.10: RMS delay spread vs. off-boresight angle combination for 38GHz. The delay spread increases as the antennas point further away from boresight.

Using highly directional, steerable antennas, a receiver is often able to establish as many as 14 links with a rooftop-mounted transmitter despite obstructions in the propagation path. The measured results, coupled with the outage study in [8], enable intelligent design of cellular base stations to fully exploit path diversity. It can be seen that a 13.3 dB horn antenna incurs less path loss than a 25 dBi horn antenna when pointing in NLOS directions or when the LOS direction is obstructed with foliage or other structures. The NLOS links have an average RMS delay spread of about 14 ns while minimal RMS delay spread was exhibited by the majority of LOS and partially obstructed LOS links. RMS delay spreads for both receiver antennas have similar CDFs, meaning the antenna beamwidth only marginally impacts the delay spread distribution. Additionally, observing the RMS delay spread as a function of the arc length (TR separation times combined angle) suggests that the RMS delay

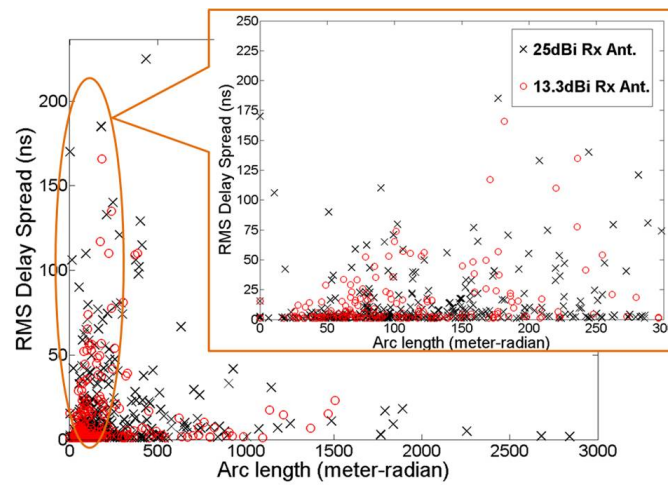


Figure 5.11: RMS delay spread vs. arc length over all 38GHz measurements. The trend is decreasing, indicating that distance prevails over angle in determining delay spread. However, a close-up of low arc lengths shows the angle playing a larger role in determining delay spread.

spread is a strong function of off-boresight angle for short links and dominated by TR separation for long links.

Chapter 6

Receiver Antenna Positioning Track

During the measurement campaigns in the spring and summer of 2011, it was clear that the measurement process is extremely tedious, especially when a large number of locations are to be measured. Also, manual steering of an antenna was not very accurate or precise. In particular, the receiver side required the most manual work when steering the receiver antenna to find angles-of-arrival that establish communication links with the transmitter. In addition, the receiver antenna must be manually moved over eight positions on a circular track for every established transmitter-receiver angle pair to find large scale fading characteristics. The idea of a motorized antenna positioning system, called the track, was quickly conceived. Reducing required manual labor, increasing precision, and saving time, such system would overcome the shortcomings of manual antenna steering procedures. The flexibility of a programmable motor controller would open vast possibilities in automating the measurement process as well.

6.1 Design

Figure 6.1 below shows how the transmitter and receiver are oriented relative to each other. When measurements are taken in the field, the researchers will manually move each track to the desired measurement locations. As concluded from discussions, the tracks will allow the researchers to finely tune the horizontal positions of the antennas to within 0.125mm accuracy, and the rotational position to within 1 degree accuracy. The total lengths of each track must be at least 30cm long, and the tracks must enable

full 360 degree antenna rotation.

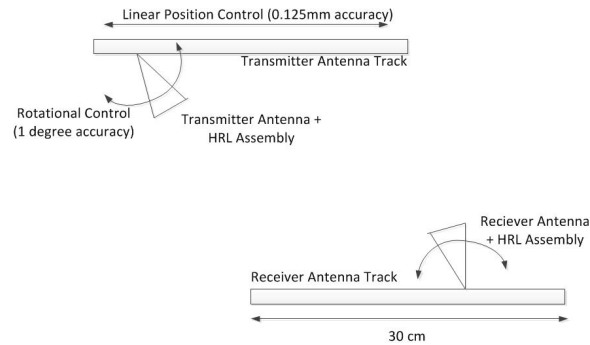


Figure 6.1: Top down view of the motorized track and their minimum required specifications.

The track will enable five degrees of freedom in the positioning of the antennas at the transmitter and receiver locations, as shown in Figure 6.2. The researchers will be able to control the horizontal position, azimuth angle, elevation angle, polarization, and height of the antennas. In these five degrees of freedom, the horizontal position and the azimuth angle control require one stepper motor each. Others degrees of freedom will be manually adjusted.

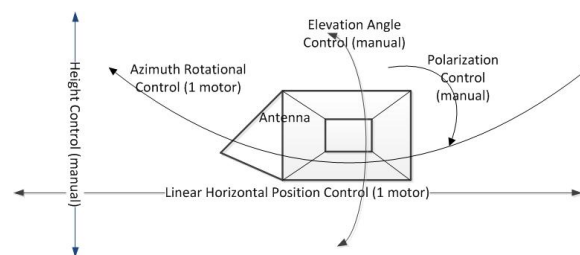


Figure 6.2: The track enables five degrees of freedom for a mounted antenna .

Constructing the track requires that the researchers attach the transmitter and receiver antenna assemblies to the track. One of the assemblies is shown in Figure 6.3. In previous measurements, the assemblies have been mounted on camera tripod heads, as shown at the bottom of Figure 6.3. Since the tripod heads enable polarization measurements and adjustment to elevation angles, the track design should provide means to attach the antennas to the track using these tripod heads.



Figure 6.3: HRL Laboratories Upconverter Assembly with horn antenna mounted on tripod head.

The detailed design of one of the tracks in Figure 6.1 is shown in Figure 6.4. Note that the motorized rotary positioner is a rotating component powered by a stepper motor, and the motorized linear positioner is a linear sliding component powered by a stepper motor. Both stepper motors will be controlled by a two-motor controller, which is itself controlled by LabVIEW on a laptop. The mechanical components of the track are organized as the following. The HRL Laboratories up/down converter assembly with antenna is first mounted on a tripod head as shown in Figure 6.3. Then, the tripod head and the motorized rotary positioner are connected through a custom adapter plate. Next, the rotary positioner is mounted on top of the motorized linear positioners carriage (the part of the linear positioner that carries the payload) using a purchased adapter plate. Finally, the motorized linear positioner is mounted on a support table.

6.2 Track Components

After searching through several possible companies, Velmex Inc. was determined to have the cheapest components for the linear positioner and rotary positioner that satisfy the design requirements. For the azimuth angle control, the B4872TS rotary positioner was purchased. The rotary positioner offers a best 0.0125° resolution and full 360° rotation and weighs 5.5 lbs. For the horizontal linear position control, the BiSlide, a linear positioner, was purchased. The positioner weighs 10 lbs and offers a best $6.35 \mu\text{m}$ resolution with a travel length of 15 inches, or 38.1 cm. Both the linear and rotary components are controlled by a Velmex two-motor controller. In addition

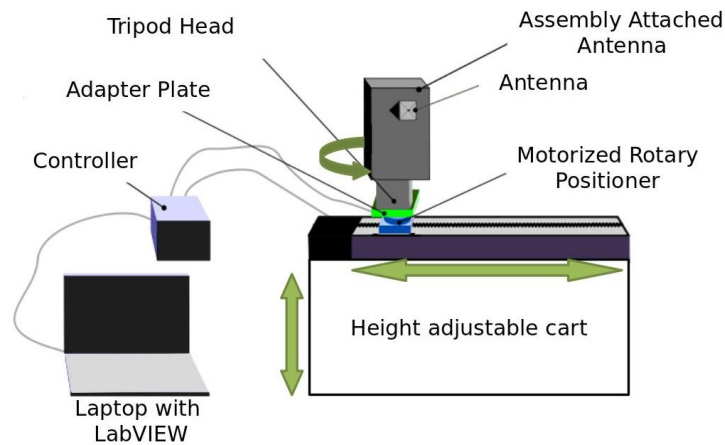


Figure 6.4: The design of the track system.

to the motorized components and their accessories, a hydraulic elevating cart from Easy Rack is also purchased. The cart enables effortless raising and lowering of the antenna while providing a platform for the motor controller. This particular cart is chosen for its lifting capability, lifting height, and light weight. Table 6.1 listed all components with their respective descriptions, quantities, and price.

Table 6.1: All the Components Purchased for the Receiver Side Antenna Positioning System. The Total Price is \$3492 not including Shipping Costs

	Description	# × \$ each
MN10-0150-E01-21 BiSlide	Travel length = 15 inches (38.1 cm), 0.00025" /step resolution. Comes standard with end limit switches (stops the motor when the carriage reaches the ends of the track).	$1 \times 822 = 822$
Vexta Type 23T2 Stepper Motor		$1 \times 155 = 155$
MC-2 Cleats	Used to secure linear positioner base. Also used to attach a second linear track	$8 \times 5 = 40$
MB-1 Bolts (10 pack)	Used to secure linear positioner base. Also used to attach a second linear track	$2 \times 3 = 6$
B4872TS Rotary Positioner	Rotary positioner, with 72:1 gear ratio stepper motor. 5°/second rotational speed. 0.0125 degrees/step rotational resolution.	$1 \times 957 = 957$
3-934-RR Zero Reference Switch	Allows the rotary positioner to return to a home position.	$1 \times 168 = 168$
MSPP-3 Adapter Plate	Connects the rotary positioner and linear track.	$1 \times 32 = 32$
Programming stepping motor control	Controls two motors with ASCII characters through RS232 standard. Enables 400 steps / motor revolution. Can connect to an additional controller using a busing cable to control a third motor.	$1 \times 816 = 816$
USB to RS232 Serial Converter	Cable used to connect the RS232 port on the motor controller and the USB ports on a laptop	$1 \times 41 = 41$
Hydraulic Elevating Cart	Elevates from 13 to 50. Self mass is 140 lbs. Supports 220 lbs (not including self mass). Platform size is 17.5x27.5. Uses double scissors structure. Hydraulically elevates platform.	$1 \times 455 = 455$

6.3 A Mechanical Concern: Torque

While choosing the track components, the torque exerted on the each was a major concern, especially when the HRL Laboratories assembly is tilted at a 90° angle, i.e. parallel to the ground. Another concern is whether critical components of the track can tolerate the mass placed on it. An analysis of the weight as well as the torque exerted on the critical track components is carried out to ensure safe operations.

The masses of each part and their maximum tolerable load normals (See Figure 6.5 for demonstration of load normal) are summarized in Table 6.2. When the tripod head is not tilted (i.e. antennas elevation angle = 0), all components can tolerate the load above them (explained below). The tripod head tolerates a maximum load of 17.6 lbs, so it can support the 2lbs HRL up/downconverter assembly above it. The rotary positioner has the adapter plate (2 lbs), the tripod head (1.9 lbs), and the HRL up/downconverter assembly (2 lbs) above it, amounting to $2.557 + 1.9 + 2 = 6.457$ lbs. This mass is much smaller than the rotary positioners tolerable mass of 200 lbs. The linear positioner has the additional mass of the rotary positioner (5.5 lbs), enduring a total of $6.457 + 5.5 = 11.957$ lbs. This mass is smaller than the linear positioners tolerable mass of 300 lbs.

Table 6.2: Self Masses and Maximum Tolerable Load Normal of Each Component

Component	Self Mass(lbs)	Max Mass Above (lbs)	Max Horizontal (Positioner is sitting flat) Load Normal (lbs)
HRL Assembly + 38GHz 25 dBi Antenna	2.557	0	No Information
Tripod Head	1.9	2.557	17.6
Custom Adapter Plate	≤ 2	4.457	No Information
Rotary Positioner	5.5	6.457	200
Purchased Adapter Plate	≤ 2	11.957	No Information
Linear Positioner	10	13.957	300
Support Table	140	23.957	220 (Uniform)

When the tripod head is tilted to change the antennas elevation angle, a horizontal

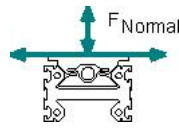


Figure 6.5: Illustration of Load Normal [16]. The normal forces are indicated by the masses with units lb (1 lb = 0.455kg).

cantilever load is endured by the rotary positioner and the linear positioner as seen in Figure 6.6. The tripod head is designed to tolerate torque produced in any orientation with a 17.6 lb load (although no maximum cantilever load information is given, the team tested the tripod heads and saw the tripod head holds the antenna when tilted 90°). The rotary positioner tolerates a maximum horizontal cantilever load of 500 in-lbF, and the linear positioner tolerates a maximum horizontal cantilever load of 500 in-lbF. In the paragraph that follows, a torque analysis is carried out to evaluate the torque experienced by the rotary positioner.

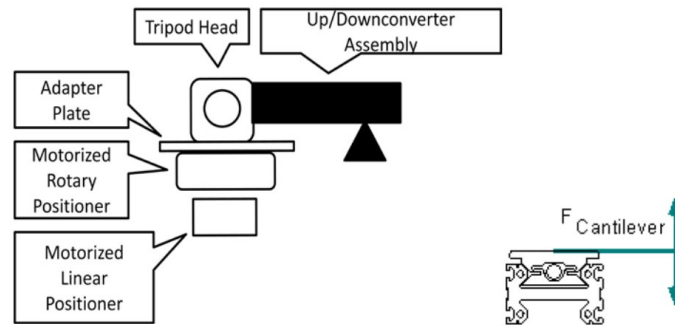


Figure 6.6: Left: Side view of the track with tripod head tilted for adjusting the elevation angle of the antenna to 90°. Right: Illustration of Cantilever force[16]. The cantilever forces are indicated with units lbF-in (1 lbF-in = 0.113 N-m).

Since the HRL up/downconverter assembly will be used in a cantilever fashion where only one end of the assembly is supported, torque calculation is important to ensure the parts (rotary and linear positioners) will work under such torque. For this analysis, the antennas elevation angle is set to 90° (chosen for ease of calculation and the largest possible angle). This results in the greatest amount of torque possible on the rotary and linear positioner at a 90° elevation angle. The analysis will make sure that in the worst case the torque exerted on the rotary and linear positioner is acceptable. Since the rotary and linear positioners are able to tolerate the same

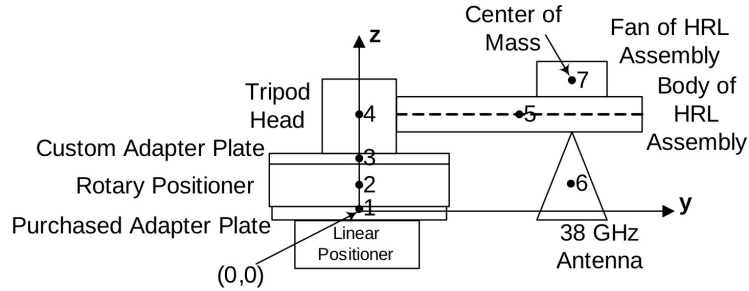


Figure 6.7: Configuration used for torque calculation. Components are numbered from 1 to 7. (0,0) indicates the intersection of the axes)

amount of horizontal cantilever load, it is enough to calculate just the torque on the linear positioner. This is because if the torque on the linear positioner is acceptable, then the torque on the rotary positioner is automatically acceptable (since rotary positioner is on top of the linear positioner, less torque is exerted on it). In Figure 23, the system is broken down into individual parts. The masses are found with a scale and the center of mass of the entire system is estimated and measured relative to the bottom of the linear positioner.

A table with the position vectors of the center of masses and the masses is made for ease of calculation. The position vectors of the centers of masses are represented in an ordered pair format (a,b) to mean $ax + by$, where \mathbf{x} and \mathbf{y} are orthonormal vectors.

Using Table 6.3, the center of gravity for all objects above the linear positioner is first calculated by:

$$\mathbf{r} = \frac{\sum m_i \times r_i (\text{inch})}{\sum m_i},$$

where m_i is the mass and r_i is the position vector of the center of gravity for the i^{th} component.

The torque exerted by the HRL up/downconverter assembly on the rotary positioner can now be found. With the center of gravity found, the torque can be found by taking the magnitude of the cross product between the position vector of the center of gravity and the weight vector \mathbf{w} :

$$|\mathbf{r} \times \mathbf{w}| = |(1.529\mathbf{y} + 2.829\mathbf{z}) \times -5.389\mathbf{z}| = 8.240 \text{ in} \cdot \text{lbF}$$

This value can be compared to the maximum tolerable torque of the rotary and

horizontal positioner, which are both 500 in-lbF.

Table 6.3: Mass and Position Vectors of Center of Masses of Components Above the Linear Positioner.

Component Number	Component Name	Position Vector (inch)	Self Mass (lb)
1	Purchased Adapter Plate	(0, 0.25)	2
2	Rotary Positioner	(0, 1.685)	5.5
3	Custom Adapter Plate	(0, 3.12)	2
4	Tripod Head	(0, 5.42)	1.9
5	HRL Assembly (Main Body)	(7.05, 5.42)	1.543
6	38 GHz Antenna	(10.711, 5.19)	0.507
7	HRL Assembly (Fan)	(9.924, 6.995)	0.507

6.4 Track Software

Physically, interfacing between the motor controller and LabVIEW is done by connecting the laptop with the motor controller via the RS232 serial port and the motor controller with the motors via four ten-foot cables. Electronically, the LabVIEW program on the laptop sends ASCII codes to the controller that communicates with the motors. Due to this simplicity, a wide array of programming languages is capable of interfacing with the controller, including LabVIEW. The motor controller comes with a LabVIEW VI (also known as subroutine) VxmDriverLV8.vi that eases the coding process.

Since the motors are controllable with LabVIEW, the code is integrated into the current digital oscilloscope code. The original LabVIEW data acquisition software front panel has been drastically improved for user-friendliness and to make room for additional virtual buttons needed by the track. Less used buttons are group together and placed on the edge. The exact configuration of the front panel is shown in the Figure 6.8. Virtual buttons are provided to control the motor movements as well as scan for signal.

Several buttons are used for initial track setup. The Show Motor Terminal turns

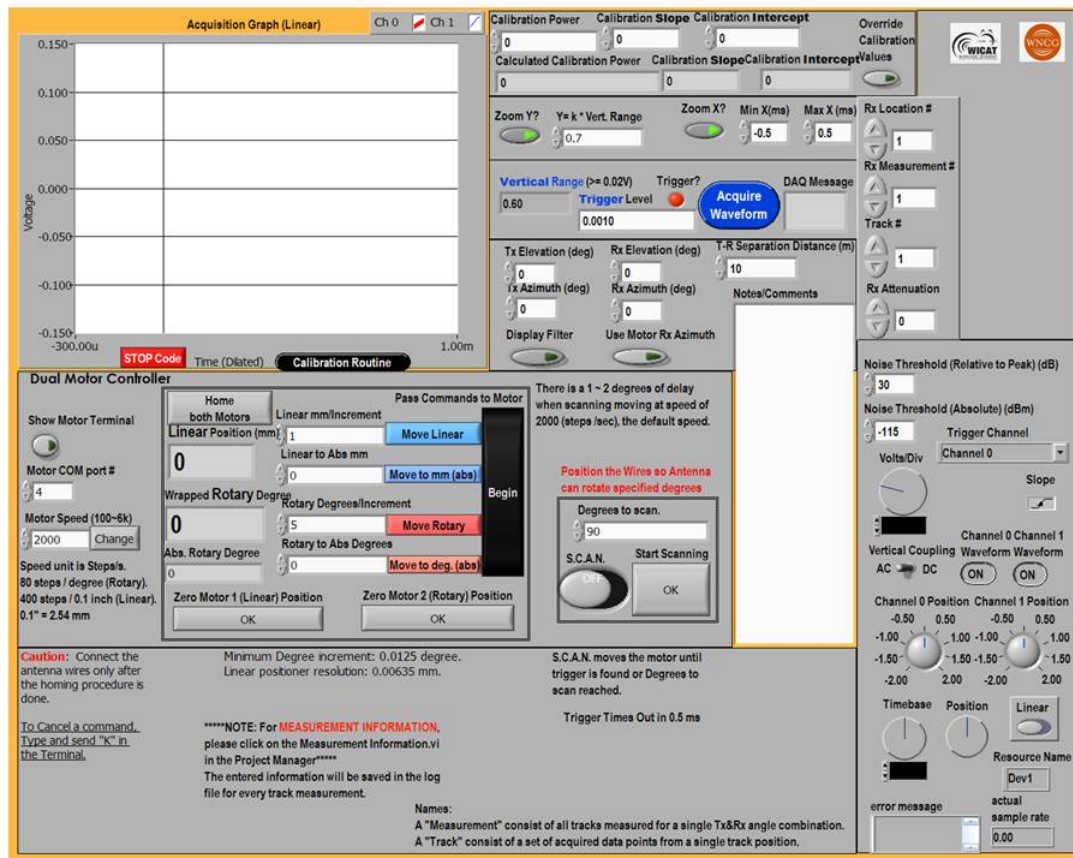


Figure 6.8: The LabVIEW front panel used to acquire data for channel sounding and control the track.

on a pop up window to display commands being sent to the motors and commands returned by the motors. The Motor COM port # input specifies the COM port used for RSC-232 to USB communication. The method for finding the exact COM port number, which can vary between computers, can be found in the documentation included with the RSC-232 to USB cable. The Motor Speed specifies the speed of the motor in units of steps/second; the speed input is bounded between 100 and 6000. Default motor speed is 2000, and the speed is reset every time the track homes.

The software also has several buttons to move the antenna with the linear and rotary positioners. These buttons are grouped in the box in the center of the Dual Motor Controller area. Note that pressing the button Pass Commands to Motor is required after selecting any button inside the box to actually send the commands to

the motor controller. This requirement does not apply to buttons not in the box.

Before starting to use the track, it is recommended to home both positioners to a starting location with the Home both Motors buttons. In this mode, the motors are set to a very slow speed to avoid damage to the limit switches, which are placed at limits of the positioners travel range to set how far the antenna travels. Due to the slow speed of the homing operation, a good idea is to move the antenna close to the proximity of the starting location first at a higher speed. The end of the homing operation resets the antenna speed to 2000.

Buttons Move Rotary and Move to deg.(abs) are made for the rotary positioner. These buttons work differently but can change the antennas azimuth angle to the same direction. Figure 25 shows how to use the two commands to move a 30° off-boresight antenna to 180° off boresight. The essential difference between the two commands is the reference angle: Move Rotarys reference angle is whatever the antenna is pointing at when the command is made; Move to deg.(abs)s reference angle is always 0°. Which command to use depends on the situation and the users preference.

The azimuth angle of the antenna is read back to the Wrapped Rotary Degree and Abs. Rotary Degree anytime there is a change. The difference between the two readings lie in that the wrapped rotary degree is modular 360, so its always between 0 and 360°, while the absolute rotary degree is a regular reading that could exceed 360°. There is one thing to be cautious about using the move rotary degree (absolute) and absolute rotary degree readings. If the current absolute rotary degree readings is more than 360°, and a small angle is entered into the move rotary degree (absolute), then the antenna can be rotated by more than 360°; wire tangling is the most dangerous aspect of this.

Buttons Move Linear and Move to mm(abs) are made for the linear positioner, which is to be used for moving the antenna to several local area positions for local area averaging. These buttons behave similarly to that of the rotary positioner. For the position reading, only an absolute position relative to position 0 is provided in Linear Position (mm), since no position wrap around can occur for the linear positioner.

Additional buttons, namely the Zero Motor 1(Linear) position and Zero Motor 2 (Rotary) position were made to make any position the linear or the rotary positioner is at position 0. This is useful if the user wants to change the homed reference position. Such situation can arise, for example, when aiming the receiver antenna to the transmitter antenna, then setting that angle as the 0° angle.

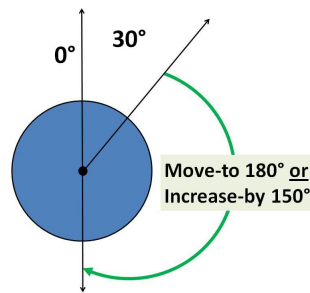


Figure 6.9: Move-Rotary and Move to Degree (absolute) commands can be used in different situations to achieve the same results.

6.5 Automatic Signal Scanning

The scan function works by detection of the no-trigger signal. Starting at a no trigger state (this can be done by steering the receiver antenna to a direction where no signal is received above the set trigger level), the software can move the azimuth angle until either of the two conditions occur: the max scan angle is reached or a trigger is found.

Scanning is executed by the Degrees to Scan, S.C.A.N., and Start Scanning, and Trigger level buttons. To enable scan mode, switch on the S.C.A.N. Degrees to Scan determines the maximum degrees the software moves the antennas azimuth angle if no signal is found. This function is made to prevent endless rotation when there is no signal at all. Start Scanning will begin to initiate the scanning process. The level of the trigger is very important to signal scanning, since it dictates whether the software sees a signal. A good trigger level to set is the minimum signal level where the system stays within the linear range. This level is determined during calibration.

Chapter 7

Future Works

All measurements in this work aimed to provide path loss and RMS delay spread statistics for one environment. More research can be done to study other parameters, such as rate of channel variation, doppler effect, and weather conditions (i.e. rain, snow, lightning). Also, measurements can be made for different environments.

The current antenna positioning track is a step toward automation, but it isn't yet fully automated. The track can be further enhanced by an automatic signal triggering algorithm. Together with the signal scanning algorithm, the track can truly be automated at least for each elevation angle. After manually setting an elevation angle, the track would be able to find a signal with the lowest trigger level possible (for the system to stay within its linear range), raise the trigger level with the trigger-setting algorithm to an appropriate level so the signal is somewhat stable, acquire data, move the antenna through a number of track positions (for local area averaging) and return, then find the next signal. The procedure will repeat until all 360° has been scanned. If the elevation angle is also motorized, then the track can find signal and measure a certain location completely by itself. The only human interaction needed would be to watch and move the equipments from location to location. When adding the elevation angle motor, it's imperative to check whether the motor can handle the torque and weight to be exerted on it. Also, special measures must be taken to avoid cable tangling during rotations.

Chapter 8

Conclusion

With the increasing demand for data rates, there is a global bandwidth shortage at current frequencies for wireless communications. For this reason, there are growing interests to use carrier frequencies greater than 30GHz to exploit the available massive amount of bandwidth. A sliding correlator was used to measure 38 GHz and 60 GHz outdoor channels in an urban campus environment in anticipation of the need for broadband propagation measurements in outdoor environments. At 60GHz, narrow-beam antennas in a campus courtyard showed adaptive beam arrays can occasionally find reflections from surrounding objects even in NLOS antenna pointing scenarios. For the peer-to-peer and peer-to-vehicle measurements, path loss exponents slightly greater than free space were found for LOS paths, while NLOS paths, when they existed, generated links that were 15 to 40dB weaker. Path loss in vehicles was much higher than the courtyard due to attenuation of the car windows, metallic body of the vehicle, and people. RMS delay spreads of up to 36 ns were observed in the courtyard for cases where transmitter and receiver antennas were not pointed at each other, but were much smaller beyond 50 m T-R separations. The mean RMS delay spread was found to be 6.02 ns for the 50 NLOS antenna pointing scenarios in this campaign. The 15 LOS antenna pointing scenarios had virtually no multipath (less than 1 ns RMS delay spread) since the main LOS signal was much stronger than the multipath. 60 GHz LOS links made with 25 dBi directional antennas are between 15 and 40 dB stronger than NLOS links, yet when the LOS path is obstructed and antennas at both the Tx and Rx are steered, the environment can sometimes offer propagation, although with more delay spread and path loss.

For rooftop-to-ground 38 GHz measurements, a receiver is often able to establish as many as 14 links with a rooftop-mounted transmitter despite obstructions in the

propagation path. The measured results, coupled with the outage study in [8], enable intelligent design of cellular base stations to fully exploit path diversity. The results shown that a 13.3 dB horn antenna incurs less path loss than a 25 dBi horn antenna when pointing in NLOS directions or when the LOS direction is obstructed with foliage or other structures. The NLOS links have an average RMS delay spread of about 14 ns while minimal RMS delay spread was exhibited by the majority of LOS and partially obstructed LOS links. RMS delay spreads for both receiver antennas have similar CDFs, meaning the antenna beamwidth only marginally impacts the delay spread distribution. Additionally, observing the RMS delay spread as a function of the arc length (TR separation times combined angle) suggests that the RMS delay spread is a strong function of off-boresight angle for short links and dominated by TR separation for long links.

An antenna positioning track presented is able to control an antenna with five degrees-of-freedom, two of which are motorized. The track was made with the aim to ease the measurement process and increase measurement accuracy. With the LabVIEW control code, the track can also scan the antennas azimuth angle to search for signals.

Future works of the research can include measuring other properties of the wireless channel, including rate of signal change from movements (doppler effect), other environments, rate of channel variation, and impact of weather on signals. The antenna positioning track can be also upgraded for complete automation.

Chapter 9

Published Works

Measurement results presented in the thesis have been published in the papers listed on this page.

- E. Ben-Dor, T.S. Rappaport, Y. Qiao, S.J. Lauffenburger, Millimeter-wave Broadband Channel Sounder and Propagation Measurements for Wireless Communications, *IEEE Globecom Conference*, pp.1-6, 5-9 Dec. 2011,
- T.S. Rappaport, E. Ben-Dor, J.N. Murdock, Y. Qiao, 38 GHz and 60 GHz Angle-dependent Propagation for Cellular & Peer-to-Peer Wireless Communications, *IEEE International Conference on Communications 2012*, in press.
- Theodore S. Rappaport, Yijun Qiao, Jonathan I. Tamir, James N. Murdock, Eshar Ben-Dor, "Cellular Broadband Millimeter Wave Propagation and Angle of Arrival for Adaptive Beam Steering Systems (Invited Paper)," *IEEE Radio Wireless Week 2012*, pp.151-154, 15-18 Jan. 2012.

Bibliography

- [1] T.S. Rappaport, J.N. Murdock, F. Gutierrez, State of the Art in 60 GHz Integrated Circuits and Systems for Wireless Communications, *Proceedings of the IEEE*, August, 2011, Vol. 99, no. 8, pp. 1390-1436.
- [2] F.J. Velez, M. Dinis, J. Fernandes, Mobile Broadband Systems: Research and Visions, *IEEE Vehicular Technology Society News*, Vol. 52, No. 2, pp. 4-12, May 2005.
- [3] J.N. Murdock, T.S. Rappaport, Consumption Factor: A Figure of Merit for Power Consumption and Energy Efficiency in Broadband Wireless Communication, *IEEE Globecom Conference 2011*, pp.1393-1398, 5-9 Dec. 2011.
- [4] S. Rajagopal, S. Abu-Surra, Z. Pi, F. Khan, Antenna Array Design for Multi-Gbps mmWave Mobile Broadband Communication, *IEEE Globecom Conference 2011*, pp.1-6, 5-9 Dec. 2011.
- [5] J. C. Liberti, T.S. Rappaport, Smart Antennas for Wireless Communications: IS-95 and Third Generation CDMA Applications. Prentice Hall PTR, Upper Saddle River, NJ, USA, 1999.
- [6] H. Xu, T.S. Rappaport, R. Boyle, J. Schaffner, Measurements and Models for 38-GHz Point-to-Multipoint Radiowave Propagation, *IEEE Journal of Selected Areas in Communications*, Vol. 18, No. 3, Mar. 2000.
- [7] E.J. Violette, R.H. Espeland, G.R. Hand, Millimeter-Wave Urban and Suburban Propagation Measurements Using Narrow and Wide Bandwidth Channel Probes, NTIA Report 85-184, Nov. 1985.
- [8] Q. Zhao, L. Jin, Rain Attenuation in Millimeter Wave Ranges, *International Symposium on Antennas, Propagation & EM Theory*, pp. 26-29, Oct. 2006.

- [9] S.Y. Seidel, H.W. Arnold, "Propagation measurements at 28 GHz to investigate the performance of local multipoint distribution service (LMDS)," *IEEE Globecom Conference*, Vol.1, pp.754-757, Nov. 1995.
- [10] P.B. Papazian, G.A. Hufford, R.J. Achatz, R. Hoffman, "Study of the local multipoint distribution service radio channel," *IEEE Transactions on Broadcasting*, Vol.43, No.2, pp.175-184, June 1997.
- [11] Z. Pi, F. Kahn, An Introduction to Millimeter-Wave Mobile Broadband systems, *IEEE Communications Magazine*, pp. 101-107, June 2011.
- [12] D. C. Cox, Delay Doppler Characteristics of Multipath Propagation at 910 MHz in a Suburban Mobile Radio Environment, *IEEE Transactions on Antennas and Propagation*, vol. Apr-20, No. 5, pp. 625-635, Sept. 1972.
- [13] W. G. Newhall, Wideband Propagation Measurement Results, Simulation Models, and Processing Techniques For a Sliding Correlator Measurement System, M.S. thesis, ECE, Virginia Tech, Blacksburg, Va, 1997.
- [14] T.S. Rappaport, S. DiPierro, R. Akturan, Analysis and Simulation of Interference to Vehicle-Equipped Digital Receivers From Cellular Mobile Terminals Operating in Adjacent Frequencies, *IEEE Transactions on Vehicular Technology*, Vol. 60, no. 4, pp. 1664-1676, May 2011.
- [15] H. Xu, V. Kukshya, T.S. Rappaport, Spatial and Temporal Characteristics of 60 GHz Indoor channels, *IEEE Journal on Selected Areas in Communications*, Vol.20, No. 3, Apr. 2002.
- [16] Velmex Inc. (2011 Dec 1), *BiSlide Model Specifications* [Online]. Available: http://www.velmex.com/bislide/motor_bislide_spec.html